Astronomy & Astrophysics

LETTER TO THE EDITOR

FAUST

XIII. Dusty cavity and molecular shock driven by IRS7B in the Corona Australis cluster

G. Sabatini[1], L. Podio[1], C. Codella[1,2], Y. Watanabe[3], M. De Simone[1,4], E. Bianchi[5], C. Ceccarelli[2],
C. J. Chandler[6], N. Sakai[7], B. Svoboda[6], L. Testi[1,8], Y. Aikawa[9], N. Balucani[10], M. Bouvier[11],
P. Caselli[12], E. Caux[13], L. Chahine[2], S. Charnley[14], N. Cuello[2], F. Dulieu[15], L. Evans[16], D. Fedele[1],
S. Feng[17], F. Fontani[1,12], T. Hama[18,19], T. Hanawa[20], E. Herbst[21], T. Hirota[22], A. Isella[23],
I. Jímenez-Serra[24], D. Johnstone[25,26], B. Lefloch[27], R. Le Gal[2,28], L. Loinard[29,30], H. B. Liu[31],
A. López-Sepulcre[2,28], L. T. Maud[4], M. J. Maureira[12], F. Menard[2], A. Miotello[4], G. Moellenbrock[6],
H. Nomura[32], Y. Oba[33], S. Ohashi[7], Y. Okoda[7,34], Y. Oya[34,35], J. Pineda[12], A. Rimola[36], T. Sakai[37],
D. Segura-Cox[38], Y. Shirley[39], C. Vastel[13], S. Viti[11], N. Watanabe[33], Y. Zhang[7],
Z. E. Zhang[40], and S. Yamamoto[41]

(Affiliations can be found after the references)

ABSTRACT

Context. The origin of the chemical diversity observed around low-mass protostars probably resides in the earliest history of these systems.
Aims. We aim to investigate the impact of protostellar feedback on the chemistry and grain growth in the circumstellar medium of multiple stellar systems.
Methods. In the context of the ALMA Large Program FAUST, we present high-resolution (50 au) observations of CH_3OH, H_2CO, and SiO and continuum emission at 1.3 mm and 3 mm towards the Corona Australis star cluster.
Results. Methanol emission reveals an arc-like structure at ∼1800 au from the protostellar system IRS7B along the direction perpendicular to the major axis of the disc. The arc is located at the edge of two elongated continuum structures that define a cone emerging from IRS7B. The region inside the cone is probed by H_2CO, while the eastern wall of the arc shows bright emission in SiO, a typical shock tracer. Taking into account the association with a previously detected radio jet imaged with JVLA at 6 cm, the molecular arc reveals for the first time a bow shock driven by IRS7B and a two-sided dust cavity opened by the mass-loss process. For each cavity wall, we derive an average H_2 column density of ∼7×10^{21} cm^{-2}, a mass of ∼9×10^{-3} $M_\odot$, and a lower limit on the dust spectral index of 1.4.
Conclusions. These observations provide the first evidence of a shock and a conical dust cavity opened by the jet driven by IRS7B, with important implications for the chemical enrichment and grain growth in the envelope of Solar System analogues.

Key words. astrochemistry – stars: formation – ISM: abundances – evolution – ISM: molecules

1. Introduction

Protostellar feedback, resulting from the complex interplay between newly forming Sun-like stars and their environment, plays a crucial role in shaping the chemical composition of the interstellar medium (ISM). The injection of energy and momentum leads to a cascade of physical and chemical processes that influence the molecular composition of the ISM (e.g. Herbst & van Dishoeck 2009; Frank et al. 2014; Ceccarelli et al. 2023, as reviews). Feedback mechanisms, including stellar winds, jets, cavities, and outflows, create a dynamic environment (e.g. shocks) that favours the enrichment of chemical species (e.g. Bachiller et al. 2001) and pave the way for the formation of interstellar complex organic molecules (iCOMs[1]; i.e. organic molecules with at least six atoms; Ceccarelli et al. 2017). Modern interferometers, such as the Atacama Large Millime-

ter/submillimeter Array (ALMA), enable astronomers to investigate these processes more thoroughly. However, so far, no clear symmetric dusty cavities opened by protostellar jets have been imaged.

In this context, the ALMA Large Program (LP) Fifty AU STudy of the chemistry in the disk/envelope system of Solar-like protostars (FAUST)[2] is designed to characterise the chemical diversity of young solar-like protostars down to a spatial resolution of ∼50 au. FAUST has shown that the chemical structure of molecular envelopes on scales of >1000 au is influenced by protostellar outflow activity (e.g. Okoda et al. 2021). New case studies are needed to further investigate the role of protostellar feedback on the different scales of envelope–disc systems.

One of the FAUST targets is the nearby Corona Australis (CrA) complex. This region has been the subject of numerous observational campaigns (e.g. Knacke et al. 1973; Harju et al. 1993; Neuhäuser & Forbrich 2008). Several Class 0/I protostars

---

[1] The lower case "i" emphasises that the term "complex" only applies in the context of the ISM.

[2] http://faust-alma.riken.jp; see Codella et al. (2021).

have been identified and characterised in terms of both their chemical (e.g. Groppi et al. 2007; Watanabe et al. 2012; Lindberg et al. 2014) and physical properties (e.g. Nutter et al. 2005; Cazzoletti et al. 2019; Sandell et al. 2021). IRS7B is the protostar at the centre of the CrA cluster, and is classified as a transitional Class 0/Class I object (Groppi et al. 2007; Watanabe et al. 2012). Recently, IRS7B was resolved into a binary system formed by IRS7B-a and IRS7B-b (Ohashi et al. 2023), both associated with discs aligned with a position angle (PA) of 115° and an inclination of ~65° (Takakuwa et al. 2024). The cluster also contains CXO 34 and IRS7A, two embedded Class I protostars, and SMM 1C (Class 0; Peterson et al. 2011; Lindberg et al. 2015). These studies also revealed prominent continuum emission from SMM 1A, observed with SCUBA-2 at 450 μm (Fig. 1; left) and located ~2000 au southwest of IRS7B; its nature is still unclear. SMM 1A has been interpreted as either a quiescent prestellar object (e.g. Nutter et al. 2005) or a filamentary structure affected by external irradiation by the Herbig Ae/Be star R-CrA (e.g. Lindberg & Jørgensen 2012; Perotti et al. 2023). The present Letter casts a new light on SMM 1A; we present an investigation of the protostellar feedback of IRS7B on the chemical properties of the ISM in the formation of multiple star–disc systems in CrA.

2. Observations and data reduction

The CrA complex was observed as part of the FAUST ALMA LP between October 2018 and September 2019 (2018.1.01205.L; PI: S. Yamamoto; Codella et al. 2021) at a resolution of ~0.''4 (~52 au at the CrA distance of 130 pc; Lindberg et al. 2014). We observed three spectral setups, one in Band 3 (85–101 GHz) and two in Band 6 (214–234 GHz and 242–262 GHz). Appendix A summarises the telescope setups for both the 12 m array and the Atacama Compact Array (ACA; Band 6 only). The average maximum recoverable scale is ~21'' (~2700 au). All observations were made with a precipitable water vapour of <2.0 mm.

The observations were centred on $(\alpha_{\rm ICRS}, \delta_{\rm ICRS})$ = (19h01m56.$^{\rm s}$42, −36°57′28.''40). The absolute flux calibration uncertainty is 10%. Data were calibrated employing the CASA pipeline 6.2.1–7 (The CASA Team 2022), including additional routines to correct for system temperature and spectral normalisation issues[3], and self-calibrated using line-free channels. The final continuum-subtracted line-cubes were cleaned (Hogbom deconvolver) with BRIGGS weighting scheme with ROBUST = 0.5 (Appendix A). The typical rms noise is ~0.08 mJy beam^{-1} for continuum and 0.8–3 mJy beam^{-1} per channel for lines. Self-calibration improved the dynamic range of the continuum maps by factors of between 3 and 10 depending on the data set. The primary beam correction was applied to all the images.

3. Results

3.1. Continuum emission

Figure 1 (central) shows the spatial distribution of dust continuum emission at 1.3 mm in the CrA field, where four compact sources are detected: IRS7B, CXO 34, IRS7A, and SMM1-C. For these sources, the position of the 1.3 mm continuum peaks derived with a 2D Gaussian fit (Appendix B) matches the coordinates reported by Lindberg et al. (2014). In addition, a fifth source (labelled FAUST-5) is detected for the first time SE

of IRS7B. No compact counterpart has been identified in the molecular lines in FAUST, suggesting a potential extragalactic origin.

More intriguingly, the continuum emission reveals the existence of two elongated structures SW of the field. These structures are detected (>3σ) up to ~1000 au (SW) and ~1700 au (S), respectively, from IRS7B. A zoom onto the central region (Fig. 1; right) shows that the two structures are symmetric with respect to the normal direction of the disc and extend along the expected direction of the outflow driven by IRS7B, with an opening angle of ~50° (dashed lines). Following Sabatini et al. (2023), we estimate the H$_2$ column density and mass of the cavity walls, assuming optically thin dust emission, a dust temperature of 30 K (Perotti et al. 2023), a standard gas-to-dust ratio of 100, and a dust opacity of $\kappa_{\rm 1.3\,mm}$= 0.9 cm^2 g^{-1} (Ossenkopf & Henning 1994), which are typical values for icy mantle dust grains and well reproduce multi-wavelength observations of low-mass star-forming regions (e.g. Evans et al. 2001; Shirley et al. 2005). The average N(H$_2$) and mass of each cavity wall are ~7 × 10^{21} cm^{-2} and ~9 × 10^{-3} $M_{\odot}$, respectively. This mass corresponds to ~0.1% of the IRS7B envelope mass estimated by van Kempen et al. (2009). Taking into account an uncertainty of 10% in the absolute flux calibration of the ALMA data, <15% in the assumed dust temperature (e.g. Sabatini et al. 2022) and ~30% for the dust opacity (e.g. Sanhueza et al. 2019), the overall uncertainty for N(H$_2$) and the mass of each cavity wall is ≲35%.

3.2. Line emission

We mapped the molecular emission of five CH$_3$OH lines, associated with a range of upper level energy, $E_{\rm up}$, from 21 K to 84 K, para-H$_2$CO (3$_{0,3}$–2$_{0,2}$), and SiO (5–4) (see Table 1). Figure 2 shows the integrated intensity maps (moment 0 maps) of the brightest lines over the velocity range [0, +12] km s^{-1}.

Figure 2a shows the spatial distribution of the CH$_3$OH-E (4$_{2,3}$–3$_{1,2}$), and reveals a molecular-arc structure that is confined within the two elongated structures detected in continuum. The arc has a length of ~3000 au and is located at a projected distance from IRS7B of ~1800 au, close to the coordinates of SMM 1A (Nutter et al. 2005; Chen & Arce 2010). Additional information is provided by the channel maps (Fig. B.1a). The methanol emission extends from +3.5 to +8.0 km s^{-1} around the systemic velocity of IRS7B ($V_{\rm sys}^{\rm IRS7B} \sim$ +6 km s^{-1}; Ohashi et al. 2023), with most of the emission at blueshifted velocities. Similar structures are traced by the other methanol lines in Figs. 2(b and c). The CH$_3$OH-A (8$_{0,8}$–7$_{1,7}$), detected in Band 3, shows several bright spots consistent with the CH$_3$OH 4$_{2,3}$–3$_{1,2}$ transition, plus fainter spots outside the Band 6 ALMA field of view (FoV; green circle in Fig. 2). This is consistent with the distribution of CH$_3$OH in Band 6 in the ACA-only maps, where the emission is recovered on a larger FoV at the expense of angular resolution (see Appendix A). In the CH$_3$OH-A (5$_{1,4}$–4$_{1,3}$) line, part of the arc structure falls outside the FoV, which is smaller at ~244 GHz compared to that at ~218 GHz. The other methanol lines with low $E_{\rm up}$ (i.e. 22 K and 28 K; Table 1) do not allow a clear identification of the arc-like structure. However, these lines are also detected at >3σ in the spectra integrated on the brightest emission peaks of the arc structure (Appendix B).

The emission from para-H$_2$CO (3$_{0,3}$–2$_{0,2}$), hereafter referred to as p-H$_2$CO, is more extended than that from methanol; it probes both the arc structure, similarly to CH$_3$OH, and an extended component confined mostly within the boundaries of

---

[3] https://help.almascience.org/index.php?/Knowledgebase/Article/View/419
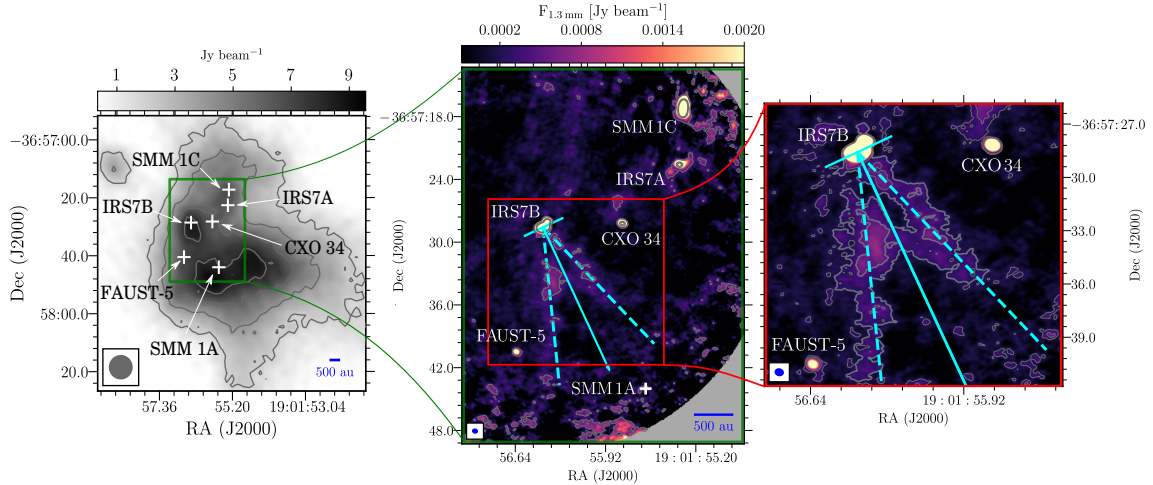
Fig. 1. Corona Australis cluster: left: SCUBA-2 map at 450 μm (JCMT archive). Contours are at $[12, 18, 30]\sigma$ where $1\sigma = 0.3$ mJy beam^{-1}; central: ALMA map of continuum emission at 1.3 mm. The first contour and steps are 6σ (0.48 mJy beam^{-1}) and 70σ, respectively. Right: Zoom onto IRS7B, where only the contours at $[3, 6]\sigma$ are shown. The detected protostellar objects are labelled. SMM 1A is not detected at 1.3 mm. The cyan line shows the PA of the IRS7B system (i.e. 115°; see text), while the arrow indicates the perpendicular direction. Dashed lines follow the elongated structures detected at 3σ. The synthesised beam is shown in the bottom-left corner of each panel.

Table 1. Properties of the lines detected towards the molecular arc in CrA.

Transitions	ν [a] (MHz)	E_{up} [a] (K)	$\log_{10}(A_{ul})$ [a] (s^{-1})	g_u [a]	δV_{chan} [a] (km s^{-1})	n_{cr} [c] (10^4 cm^{-3})	$\int I$ [K km s^{-1}] [a] "A"	"B"	"C"
CH$_3$OH-A $(8_{0,8}\text{-}7_{1,7})$	95 169.391	84	−5.37	68	1.54	1.3–1.4	8.6	4.1	6.1
CH$_3$OH-A $(2_{1,2}\text{-}1_{1,1})$	95 914.310	22	−5.60	20	1.54	2.0–2.1	4.1	1.8	3.9
CH$_3$OH-A $(3_{1,3}\text{-}4_{0,4})$	107 013.831	28	−5.51	28	0.17	3.2–3.5	4.5	<2.6	2.8
SiO $(5\text{-}4)$	217 104.980	31	−3.28	11	0.51	153.1–156.1	1.2	3.7	<0.6
CH$_3$OH-E $(4_{2,3}\text{-}3_{1,2})$	218 440.063	46	−4.33	36	0.17	24.3–23.4	19.2	8.6	9.2
p-H$_2$CO $(3_{0,3}\text{-}2_{0,2})$	218 222.192	21	−3.55	7	0.17	160.1–183.0	14.3	8.9	17.9
CH$_3$OH-A $(5_{1,4}\text{-}4_{1,3})$	243 915.788	50	−4.22	44	0.15	19.9–21.1	–	6.9	3.9

Notes. [a]Spectroscopic data from The Cologne Database for Molecular Spectroscopy (Müller et al. 2005). [b]The SiO (5–4) spectrum is smoothed in velocity by a factor of three to increase sensitivity. [c]Critical densities obtained considering downward collision rates in a multilevel system and a temperature range of 50–100 K (Sect. 3.3). Collisional rates taken from the LAMDA database (Schöier et al. 2005), based on Balança et al. (2018) for SiO, Wiesenfeld & Faure (2013) for p-H$_2$CO and Rabli & Flower (2010) for the A- and E-type CH$_3$OH. [d]We assume an uncertainty of 20%. Regions "A", "B", and "C" are centred at the peak positions of CH$_3$OH $(4_{2,3}\text{–}3_{1,2})$, SiO (5–4), and p-H$_2$CO $(3_{0,3}\text{–}2_{0,2})$, respectively (see Fig. 2).

the cone probed by the dust at 1.3 mm (Fig. 2d). The channel maps show that, at redshifted velocities and close to V_{sys}^{IRS7B}, the p-H$_2$CO emission is extended over a large portion of the FoV, and therefore it is likely contaminated by envelope emission, while it follows the methanol distribution at blueshifted velocities (Fig. B.1b), revealing arc structures.

The SiO (5–4) moment 0 map reveals two emitting regions (Fig. 2e): the first overlaps on the SW side of the molecular arc traced by CH$_3$OH and H$_2$CO; the second is located at the edge of the FoV, beyond the CH$_3$OH molecular arc, at a distance of >2100 au from IRS7B. The channel maps show that SiO has the predominant emission component in the blueshifted regime similarly to CH$_3$OH and H$_2$CO (Fig. B.2). This suggests that the blueshifted emission of SiO is also associated with the arc-structure revealed by CH$_3$OH and H$_2$CO (see Sect. 5).

3.3. Physical properties of the molecular arc

To determine the physical conditions of the emitting gas in the molecular arc, we extracted the spectra of all the observed

lines at three positions along the arc structure, labelled "A", "B", and "C", and centred at the peak positions of CH$_3$OH $(4_{2,3}\text{–}3_{1,2})$, SiO (5–4), and p-H$_2$CO $(3_{0,3}\text{–}2_{0,2})$, respectively (Fig. 2). Each region has an equivalent area of nine ALMA beams. The spectra and the line fitting are discussed in Appendix B.

Assuming local thermodynamic equilibrium (LTE) and optically thin emission, we constructed rotational diagrams (RDs) to quantify the column density, N_{tot}, and the rotational temperature, T_{rot}, of CH$_3$OH (Fig. 3) observed in the "A", "B", and "C" positions. It is assumed that the methanol A/E ratio is equal to unity, which is a good approximation for temperatures of >20 K (Wirström et al. 2011; Carney et al. 2019). We derived the critical densities of the observed lines (Table 1) assuming a temperature range of 50–100 K and taking into account downward collision rates in a multi-level system (see Draine 2011). The critical densities range from 10^4 cm^{-3} to ~2×10^6 cm^{-3} – below the average H$_2$ number densities determined for SMM 1A (i.e. 10^6 cm^{-3}; Lindberg & Jørgensen 2012) – which supports the assumption of LTE conditions. The RD analysis is obtained
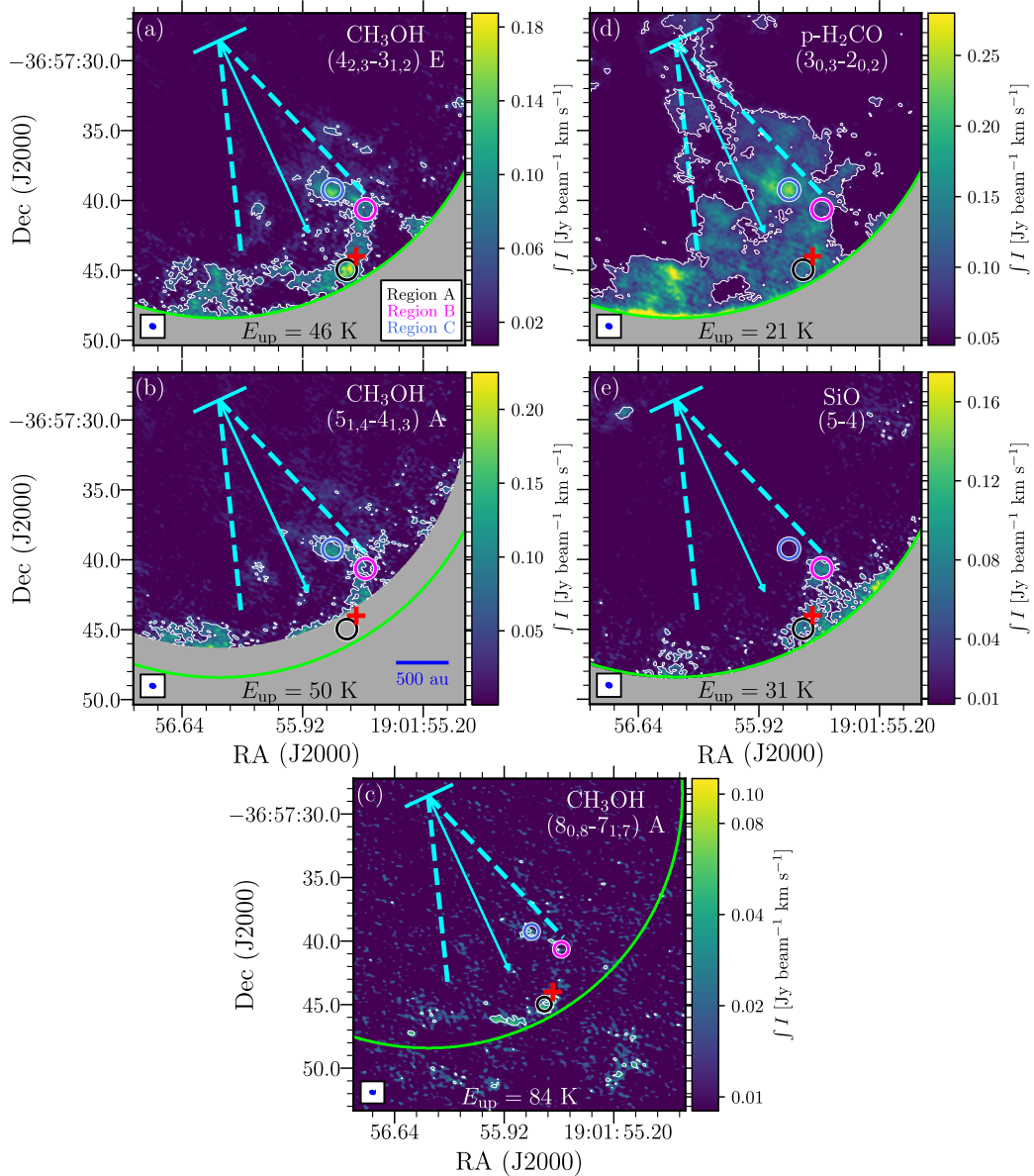
Fig. 2. Moment 0 of (a) CH$_3$OH-E ($4_{2,3}$–$3_{1,2}$), (b) CH$_3$OH-A ($5_{1,4}$–$4_{1,3}$), (c) CH$_3$OH-A ($8_{0,8}$–$7_{1,7}$), (d) p-H$_2$CO ($3_{0,3}$–$2_{0,2}$), and (e) SiO (5–4) lines around the molecular arc (integrated from 0 to +12 km s^{-1}). Cyan lines and arrows follow Fig. 1. The white contours mark the 5σ emission. Small circles indicate the positions of the brightest spots in CH$_3$OH ($4_{2,3}$–$3_{1,2}$), SiO (5–4), and p-H$_2$CO ($3_{0,3}$–$2_{0,2}$), which we label "A", "B", and "C", respectively. The red cross indicates the position of SMM 1A (Fig. 1). The green semicircle shows the ALMA Band 6 FoV, while the grey background delimits the region inside each ALMA pointing.

using the line intensity integrated on the blueshifted arc component. Taking into account the calibration uncertainty and the rms of the lines spectra, the errors on the integrated intensities is ~20%. The methanol $N_{\rm tot}^{\rm CH_3OH}$ are between $6 \pm 2 \times 10^{15}$ cm^{-2} and $16 \pm 3 \times 10^{15}$ cm^{-2}, with $T_{\rm rot}$ of ~50–60 K. In region "A", where methanol peaks, we performed a non-LTE large velocity gradient (LVG) analysis using the grelvg code (Ceccarelli et al. 2003). The resulting $T_{\rm rot,LVG}$ ~ 70–90 K and $N_{\rm tot,LVG}^{\rm CH_3OH}$ ~ 2–6×10^{15} cm^{-2} are in agreement with those derived from the RDs. Indeed the derived line opacities ($\tau < 0.5$) and gas densities (~2×10^7 cm^{-3}) support the LTE and optically thin RD assumptions. Our results are consistent with the previous estimate by Perotti et al. (2023), who observed SMM 1A, combining Submillimeter Array (SMA) and Atacama Pathfinder Experiment (APEX) observations, and assuming a $T_{\rm rot}$ ~30 K.

Assuming the same range of $T_{\rm rot}$ as that obtained for CH$_3$OH, we derive $N_{\rm tot}^{\rm H_2CO} \simeq 0.8$–$2 \times 10^{14}$ cm^{-2}. Our $N_{\rm tot}^{\rm H_2CO}$ values are approximately consistent with the values reported for SMM 1A by Lindberg & Jørgensen (2012), 10^{13}–10^{14} cm^{-2}, which are based on SMA/APEX observations with a resolution of ~6″ × 3″, and a $T_{\rm rot}$ ~ 48 K. Finally, we derived the total column density of SiO, a typical shock-induced sputtering tracer (see Sect. 4), assuming a temperature range of 50–150 K (e.g. Podio et al. 2021), obtaining $N_{\rm tot}^{\rm SiO} = 1$–$3\times 10^{13}$ cm^{-2} towards the SiO emitting peak (B). The estimated $N_{\rm tot}$, as well as the [CH$_3$OH]/[SiO] and [CH$_3$OH]/[H$_2$CO] abundance ratios (~250–600, and ~40–130, respectively), are in agreement with the values derived in shocked regions around low-mass protostars (e.g. Bachiller & Pérez Gutiérrez 1997; Cuadrado et al. 2017; Podio et al. 2021; De Simone et al. 2022).
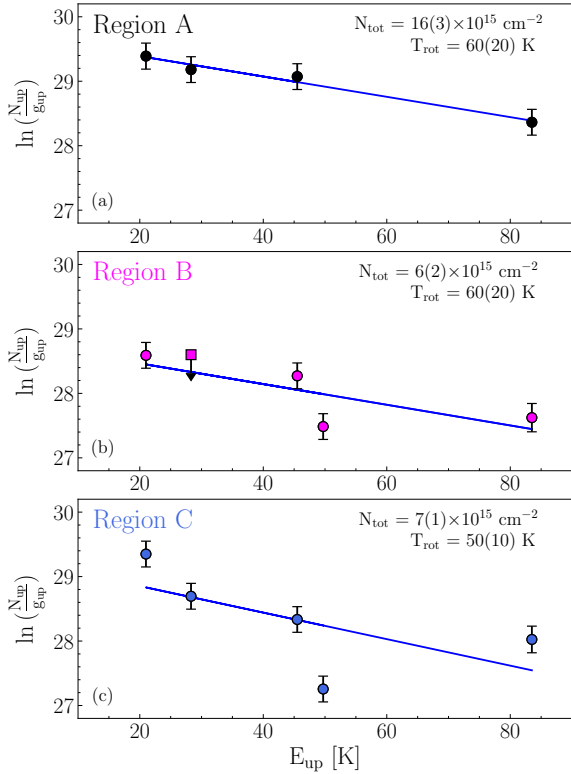
Fig. 3. Rotational diagrams of the CH$_3$OH lines (Fig. B.3) for Region: A (in black), B (in magenta), and C (in pale blue). The best-fit values of $T_{\rm rot}$ and total column density are reported.

4. Discussion

The ALMA-FAUST data reveal an extended molecular arc-structure traced by CH$_3$OH, where emission due to H$_2$CO and SiO has also been detected. The arc is located in the SW region of the CrA cluster and matches the coordinates of SMM 1A. The RD analysis of the CH$_3$OH lines supports that the arc is a coherent structure with relatively constant $N_{\rm tot}^{\rm CH_3OH}$ and $T_{\rm rot}^{\rm CH_3OH}$. The H$_2$CO distribution shows that the arc is connected to the IRS7B system at the CrA cluster centre.

4.1. Physical origin of the molecular arc in CrA

Methanol is one of the most abundant iCOMs detected in star-forming regions and is considered a key precursor of many pre-biotic compounds in space (e.g. Herbst & van Dishoeck 2009; Ceccarelli et al. 2023). The main chemical process for synthesising CH$_3$OH is CO hydrogenation on grains, in which CO is converted to H$_2$CO and then to methanol. This process is extremely efficient in solid phase during the early stages of star formation (e.g. Watanabe & Kouchi 2002; Fuchs et al. 2009; Santos et al. 2022) when the gas temperatures are <20 K, $n(\rm H_2) > 10^4\,cm^{-3}$, and CO is strongly depleted at the surface of dust grains (e.g. Caselli et al. 1999; Bergin et al. 2002; Sabatini et al. 2019, 2021, 2022). The detection of methanol in the arc-structure in CrA can be associated with either (i) external irradiation (see e.g. Cuadrado et al. 2017) or (ii) shocked regions (e.g. Ceccarelli et al. 2023, and references therein).

The first interpretation was proposed by Lindberg & Jørgensen (2012), who derived a map of H$_2$CO rotational temperature based on SMA/APEX observations with a resolution of 6″×3″. The authors found $T_{\rm rot}^{\rm H_2CO}$ in the 60–100 K range, and

interpreted this high value as a consequence of external illumination by the Herbig Ae/Be star R CrA located at ∼50″ in the NW direction (i.e. ∼6500 au at the cluster distance). The interstellar radiation field in SMM 1A would increase by a factor of 750–3000 when assuming a luminosity of 100–200 $L_\odot$ for R CrA, respectively. This picture is in agreement with the recent estimates of Sissa et al. (2019), who report an R CrA luminosity of ∼130 $L_\odot$, and with the relatively small full width at half maximums (FWHMs) of the CH$_3$OH and H$_2$CO lines (<1.2 km s^{-1}) fitted in Fig. B.3. Nevertheless, the 50 au angular resolution of the FAUST data enabled us to resolve the arc structure with unprecedented accuracy, that is, a factor of ∼10 greater accuracy than in Lindberg & Jørgensen (2012). The newly discovered arc morphology found in SMM 1A would suggest a source of illumination in the southwest (outside the ALMA FoV) or in the cluster centre. Remarkably, no major illumination source is found in either direction, as only the IRS7B system ($L_{\rm bol} \sim$ 4.6 $L_\odot$; Lindberg et al. 2014) and the prestellar source SMM 1As ($L_{\rm bol} \sim 0.04\,L_\odot$; Sicilia-Aguilar et al. 2013) have been reported in the literature within 50″ of SMM 1A.

On the other hand, the SiO detection at the edge of the CH$_3$OH arc supports the second scenario, in which the arc is the fingerprint of a shocked region. Indeed, SiO is mainly formed by the shock-induced sputtering and/or shattering of the grain mantles and refractory cores (e.g. Caselli et al. 1997; Gusdorf et al. 2008a,b; Jiménez-Serra et al. 2008; Guillet et al. 2011). In this case, the arc-shape suggests the occurrence of a jet driven by IRS7B towards the SW. Moreover, the molecular arc revealed by FAUST is blueshifted, in agreement with the disc flaring reported by Takakuwa et al. (2024), indicating that the near disc-side is to the NE, and therefore the blueshifted jet is towards the SW.

Evidence of outflowing material in CrA was first suggested by Levreault (1988) based on ^{12}CO (2–1) data collected with the Millimeter Wave Observatory (MWO). Although the coarse resolution of the MWO (1″3) prevented the identification of the driving source(s), the blueshifted wing of the outflow is aligned along the direction connecting IRS7B with SMM 1A. Radio continuum observations with ATCA[4] at 3, 6, and 20 cm revealed a bipolar structure in the NE-SW direction centred on IRS7B (Harju et al. 2001; Choi et al. 2008; Miettinen et al. 2008). More recently, Liu et al. (2014) also reported an extended (∼70″ in the SMM 1A direction) bipolar radio jet detected at 3.5 cm with the *Karl G. Jansky* Very Large Array (JVLA; beam ∼4″ × 2″). In Fig. 4 (left panel), we show the JVLA map (green contours; Liu et al. 2014) superimposed on the SCUBA-2 map at 450 μm (grey scale[5]). What originally appeared in the SCUBA-2 data as an overdensity of cold gas (e.g. Nutter et al. 2005; Chen et al. 2010) overlaps with both (a) the direction of propagation of the radio-jet discovered by Liu et al. (2014) and (b) the molecular arc traced by methanol (see Fig. 4, right). Moreover, the region in which the radio-jet would collide with the arc also corresponds to the zone in which the $T_{\rm rot}^{\rm H_2CO}$ derived in Lindberg & Jørgensen (2012) reaches its maximum values. In conclusion, based on the arc-shape, the association with the radio jet detected at centimetre wavelengths, and the detection of a typical shock tracer, namely SiO, we conclude that the observed molecular arc is most likely the signature of a bow-shock driven by IRS7B.

---

[4] Australia Telescope Compact Array (ATCA).
[5] Reduced data can be found at the Canadian Astronomy Data Centre (Project-ID: MJLSG35; https://www.cadc-ccda.hia-iha.nrc-cnrc.gc.ca/en/search/).
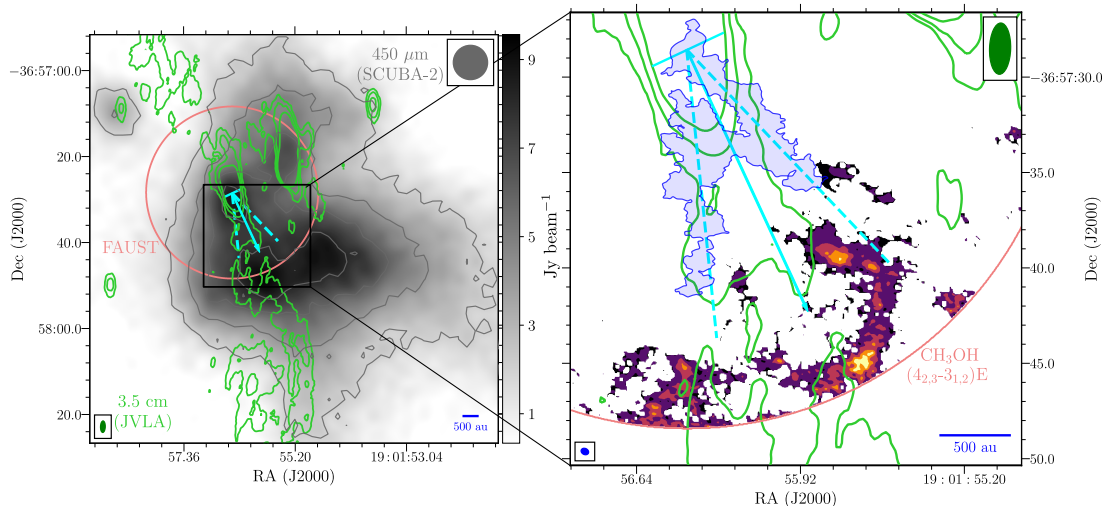
Fig. 4. Comparison between JVLA, SCUBA, and ALMA-FAUST observations in CrA: Left: JVLA 3.5 cm map (green contours; Liu et al. 2014) superimposed on the SCUBA-2 map at 450 μm (colour map and grey contours; JCMT archive). The green contours are at [5, 10, 20]σ where $1\sigma = 8\,\mu$Jy beam^{-1}, whilst the grey ones are the same as Fig. 1. Right: Zoom onto the arc (Fig. 2a). The blue-shaded area marks the 3σ thermal dust continuum emission taken from Fig. 1. The ALMA, JVLA, and SCUBA beams are shown in these panels in blue, green, and grey, respectively.

4.2. First imaging of symmetric dusty cavity walls

In light of these findings, the "V"-shaped structure detected in continuum (Fig. 4, right) traces the dust emission from the cavity walls opened by the IRS7B outflow. This is in agreement with the direction of the JVLA radio jet with the orientation of the cavity observed by ALMA (Fig. 4). To our knowledge, this is the first imaging of symmetric cavity walls of dust opened by a jet (on scales of 50 au) in a low-mass star-forming system.

This provides a unique opportunity to study the dust properties at the edge of an outflow cavity. Under the Rayleigh–Jeans approximation, both the size and the properties of interstellar dust grains can be inferred from the spectral index of the dust spectral energy distribution at (sub)millimetre wavelengths (α). We measure α in the cavity walls using Band 6 (1.3 mm) and Band 3 (3 mm) continuum maps. In Band 3, the cavity walls are not detected, and so we derive a lower limit $\alpha > 1.4$.

The spectral index for typical ISM grains is $\alpha_{\rm ISM} \sim 3.7$ (Testi et al. 2014), while low values (down to $\alpha \sim 1.5$) have been observed in the inner few hundred astronomical units (au) around Class 0/I sources. Low α values can be due to dust growth (e.g. Chiang et al. 2012; Miotello et al. 2014; Galametz et al. 2019), while recent theoretical calculations and observations show that large grains in the envelope may be the result of transport from the site of growth, the inner dense disc, to the envelope via magnetohydrodynamical (MHD) winds (Wong et al. 2016; Giacalone et al. 2019; Tsukamoto et al. 2021; Cacciapuoti et al. 2024). In this context, the estimated $\alpha > 1.4$ allows the possibility that high-density cavity walls, like those in CrA, are the sites for in situ dust growth in protostellar envelopes.

5. Conclusions

In this Letter, we present high-resolution (50 au) observations of continuum (1.3 mm and 3 mm) and molecular (CH$_3$OH, H$_2$CO and SiO) emission towards the CrA cluster in the context of the ALMA FAUST LP. Our analysis indicates that SMM 1A, previously identified as an extended continuum structure, is associated with a shock driven by IRS7B, and mapped in CH$_3$OH, H$_2$CO, and SiO, and with a conical dusty cavity opened by the mass-loss process. We estimated the H$_2$ column density

($\sim 7 \times 10^{21}$ cm^{-2}) and mass ($\sim 9 \times 10^{-3}$ $M_\odot$) in the cavity walls, and a lower limit for the dust spectral index ($\alpha > 1.4$), which could imply the presence of millimetre-sized grains. Based on these results, we conclude that the CrA cluster may be a unique laboratory with which to investigate and test models of dust grain growth in the envelope.

Additional higher-sensitivity and higher-resolution observations of shock tracers, such as SiO and CO, are needed to reveal the IRS7B jet. The discovery of a twin system in IRS7B (Ohashi et al. 2023) opens the possibility that there are two jets. Therefore, the SiO knot could be due to precession. Further mapping of CH$_3$OH emission in the SW region around SMM 1A and beyond the FAUST FoV is also needed to reveal additional interactions between the jet and the CrA envelope on a larger scale; our Band-3 maps already suggest their existence. This would allow us to determine the extent to which the jet influences the chemical composition of the CrA cluster. Ultimately, a more accurate estimate of α will be made possible with more sensitive observations at longer wavelengths, allowing us to constrain the properties and size distribution of the dust grains in the cavity walls and to probe for the formation and/or entrainment of large grains in the envelope.

References

Bachiller, R., & Pérez Gutiérrez, M. 1997, ApJ, 487, L93

Bachiller, R., Pérez Gutiérrez, M., Kumar, M. S. N., & Tafalla, M. 2001, A&A, 372, 899

Balança, C., Dayou, F., Faure, A., Wiesenfeld, L., & Feautrier, N. 2018, MNRAS, 479, 2692

Bergin, E. A., Alves, J., Huard, T., & Lada, C. J. 2002, ApJ, 570, L101

Cacciapuoti, L., Testi, L., Podio, L., et al. 2024, ApJ, 961, 90

Carney, M. T., Hogerheijde, M. R., Guzmán, V. V., et al. 2019, A&A, 623, A124

Caselli, P., Hartquist, T. W., & Havnes, O. 1997, A&A, 322, 296

Caselli, P., Walmsley, C. M., Tafalla, M., Dore, L., & Myers, P. C. 1999, ApJ, 523, L165

Cazzoletti, P., Manara, C. F., Baobab Liu, H., et al. 2019, A&A, 626, A11

Ceccarelli, C., Maret, S., Tielens, A. G. G. M., Castets, A., & Caux, E. 2003, A&A, 410, 587

Ceccarelli, C., Caselli, P., Fontani, F., et al. 2017, ApJ, 850, 176

Ceccarelli, C., Codella, C., Balucani, N., et al. 2023, in Organic Chemistry in the First Phases of Solar-Type Protostars, eds. S. Inutsuka, Y. Aikawa, T. Muto, K. Tomida, & M. Tamura (San Francisco: Astronomical Society of the Pacific), ASP Conf. Ser., 534, 379

Chen, X., & Arce, H. G. 2010, ApJ, 720, L169

Chen, H.-R., Liu, S.-Y., Su, Y.-N., & Zhang, Q. 2010, ApJ, 713, L50

Chiang, H.-F., Looney, L. W., & Tobin, J. J. 2012, ApJ, 756, 168

Choi, M., Hamaguchi, K., Lee, J.-E., & Tatematsu, K. 2008, ApJ, 687, 406

Codella, C., Ceccarelli, C., Chandler, C., et al. 2021, Front. Astron. Space Sci., 8, 227

Cuadrado, S., Goicoechea, J. R., Cernicharo, J., et al. 2017, A&A, 603, A124

De Simone, M., Codella, C., Ceccarelli, C., et al. 2022, MNRAS, 512, 5214

Draine, B. T. 2011, Physics of the Interstellar and Intergalactic Medium (Princeton University Press)

Evans, N. J., II, Rawlings, J. M. C., Shirley, Y. L., & Mundy, L. G. 2001, ApJ, 557, 193

Frank, A., Ray, T. P., Cabrit, S., et al. 2014, in Protostars and Planets VI, eds. H. Beuther, R. S. Klessen, C. P. Dullemond, & T. Henning (Tucson: University of Arizona Press), 451

Fuchs, G. W., Cuppen, H. M., Ioppolo, S., et al. 2009, A&A, 505, 629

Galametz, M., Maury, A. J., Valdivia, V., et al. 2019, A&A, 632, A5

Giacalone, S., Teitler, S., Königl, A., Krijt, S., & Ciesla, F. J. 2019, ApJ, 882, 33

Ginsburg, A., Sokolov, V., de Val-Borro, M., et al. 2022, AJ, 163, 291

Groppi, C. E., Hunter, T. R., Blundell, R., & Sandell, G. 2007, ApJ, 670, 489

Guillet, V., Pineau Des Forêts, G., & Jones, A. P. 2011, A&A, 527, A123

Gusdorf, A., Cabrit, S., Flower, D. R., & Pineau Des Forêts, G. 2008a, A&A, 482, 809

Gusdorf, A., Pineau Des Forêts, G., Cabrit, S., & Flower, D. R. 2008b, A&A, 490, 695

Harju, J., Haikala, L. K., Mattila, K., et al. 1993, A&A, 278, 569

Harju, J., Higdon, J. L., Lehtinen, K., & Juvela, M. 2001, in Science with the Atacama Large Millimeter Array, ASP Conf. Ser., 235, 125

Herbst, E., & van Dishoeck, E. F. 2009, ARA&A, 47, 427

Jiménez-Serra, I., Caselli, P., Martín-Pintado, J., & Hartquist, T. W. 2008, A&A, 482, 549

Knacke, R. F., Strom, K. M., Strom, S. E., Young, E., & Kunkel, W. 1973, ApJ, 179, 847

Levreault, R. M. 1988, ApJS, 67, 283

Lindberg, J. E., & Jørgensen, J. K. 2012, A&A, 548, A24

Lindberg, J. E., Jørgensen, J. K., Brinch, C., et al. 2014, A&A, 566, A74

Lindberg, J. E., Jørgensen, J. K., Watanabe, Y., et al. 2015, A&A, 584, A28

Liu, H. B., Galván-Madrid, R., Forbrich, J., et al. 2014, ApJ, 780, 155

Miettinen, O., Kontinen, S., Harju, J., & Higdon, J. L. 2008, A&A, 486, 799

Miotello, A., Testi, L., Lodato, G., et al. 2014, A&A, 567, A32

Müller, H. S. P., Schlöder, F., Stutzki, J., & Winnewisser, G. 2005, J. Mol. Struct., 742, 215

Neuhäuser, R., & Forbrich, J. 2008, in Handbook of Star Forming Regions, Volume II, ed. B. Reipurth, 5, 735

Nutter, D. J., Ward-Thompson, D., & André, P. 2005, MNRAS, 357, 975

Ohashi, N., Tobin, J. J., Jørgensen, J. K., et al. 2023, ApJ, 951, 8

Okoda, Y., Oya, Y., Francis, L., et al. 2021, ApJ, 910, 11

Ossenkopf, V., & Henning, T. 1994, A&A, 291, 943

Perotti, G., Jørgensen, J. K., Rocha, W. R. M., et al. 2023, A&A, 678, A78

Peterson, D. E., o Garatti, A. C., Bourke, T. L., et al. 2011, ApJS, 194, 43

Podio, L., Tabone, B., Codella, C., et al. 2021, A&A, 648, A45

Rabli, D., & Flower, D. R. 2010, MNRAS, 406, 95

Sabatini, G., Giannetti, A., Bovino, S., et al. 2019, MNRAS, 490, 4489

Sabatini, G., Bovino, S., Giannetti, A., et al. 2021, A&A, 652, A71

Sabatini, G., Bovino, S., Sanhueza, P., et al. 2022, ApJ, 936, 80

Sabatini, G., Bovino, S., & Redaelli, E. 2023, ApJ, 947, L18

Sandell, G., Reipurth, B., Vacca, W. D., & Bajaj, N. S. 2021, ApJ, 920, 7

Sanhueza, P., Contreras, Y., Wu, B., et al. 2019, ApJ, 886, 102

Santos, J. C., Chuang, K.-J., Lamberts, T., et al. 2022, ApJ, 931, L33

Schöier, F. L., van der Tak, F. F. S., van Dishoeck, E. F., & Black, J. H. 2005, A&A, 432, 369

Shirley, Y. L., Nordhaus, M. K., Grcevich, J. M., et al. 2005, ApJ, 632, 982

Sicilia-Aguilar, A., Henning, T., Linz, H., et al. 2013, A&A, 551, A34

Sissa, E., Gratton, R., Alcalà, J. M., et al. 2019, A&A, 630, A132

Takakuwa, S., Saigo, K., Kido, M., et al. 2024, ApJ, 964, 24

Testi, L., Birnstiel, T., Ricci, L., et al. 2014, in Protostars and Planets VI, eds. H. Beuther, R. S. Klessen, C. P. Dullemond, & T. Henning (Tucson: University of Arizona Press), 339

The CASA Team (Bean, B., et al.) 2022, PASP, 134, 114501

Tsukamoto, Y., Machida, M. N., & Inutsuka, S. 2021, ApJ, 913, 148

van Kempen, T. A., van Dishoeck, E. F., Hogerheijde, M. R., & Güsten, R. 2009, A&A, 508, 259

Watanabe, N., & Kouchi, A. 2002, ApJ, 571, L173

Watanabe, Y., Sakai, N., Lindberg, J. E., et al. 2012, ApJ, 745, 126

Wiesenfeld, L., & Faure, A. 2013, MNRAS, 432, 2573

Wirström, E. S., Geppert, W. D., Hjalmarson, Å., et al. 2011, A&A, 533, A24

Wong, Y. H. V., Hirashita, H., & Li, Z.-Y. 2016, PASJ, 68, 67

[1] INAF, Osservatorio Astrofisico di Arcetri, Largo E. Fermi 5, 50125 Firenze, Italy
e-mail: giovanni.sabatini@inaf.it

[2] Univ. Grenoble Alpes, CNRS, IPAG, 38000 Grenoble, France

[3] Materials Science and Engineering, College of Engineering, Shibaura Institute of Technology, 3-7-5 Toyosu, Koto-ku, Tokyo 135-8548, Japan

[4] European Southern Observatory, Karl-Schwarzschild Str. 2, 85748 Garching bei München, Germany

[5] Excellence Cluster ORIGINS, Boltzmannstraße, 2D-85748 Garching, Germany

[6] National Radio Astronomy Observatory, PO Box O, Socorro, NM 87801, USA

[7] RIKEN Cluster for Pioneering Research, 2-1, Hirosawa, Wako-shi, Saitama 351-0198, Japan

[8] Dipartimento di Fisica e Astronomia "Augusto Righi", Viale Berti Pichat 6/2, Bologna, Italy

[9] Department of Astronomy, The University of Tokyo, 7-3-1 Hongo, Bunkyo-ku, Tokyo 113-0033, Japan

[10] Department of Chemistry, Biology, and Biotechnology, The University of Perugia, Via Elce di Sotto 8, 06123 Perugia, Italy

[11] Leiden Observatory, Leiden University, PO Box 9513, 2300 RA Leiden, The Netherlands

[12] Center for Astrochemical Studies, Max-Planck-Institut für extraterrestrische Physik (MPE), Gieenbachstr. 1, 85741 Garching, Germany

[13] IRAP, Univ. de Toulouse, CNRS, CNES, UPS, Toulouse, France

[14] Astrochemistry Laboratory, Code 691, NASA Goddard Space Flight Center, 8800 Greenbelt Road, Greenbelt, MD 20771, USA

[15] CY Cergy Paris Université, Sorbonne Université, Observatoire de Paris, PSL University, CNRS, LERMA, 95000 Cergy, France

[16] School of Physics and Astronomy, University of Leeds, Leeds LS2 9JT, UK

[17] Department of Astronomy, Xiamen University, Xiamen, Fujian 361005, PR China

[18] Komaba Institute for Science, The University of Tokyo, 3-8-1 Komaba, Meguro, Tokyo 153-8902, Japan

[19] Department of Basic Science, The University of Tokyo, 3-8-1 Komaba, Meguro, Tokyo 153-8902, Japan

[20] Center for Frontier Science, Chiba University, 1-33 Yayoi-cho, Inage-ku, Chiba 263-8522, Japan

[21] Department of Chemistry, University of Virginia, McCormick Road, PO Box 400319, Charlottesville, VA 22904, USA

[22] National Astronomical Observatory of Japan, Osawa 2-21-1, Mitaka-shi, Tokyo 181-8588, Japan

[23] Department of Physics and Astronomy, Rice University, 6100 Main Street, MS-108 Houston, TX 77005, USA

[24] Centro de Astrobiologíña (CSIC-INTA), Ctra. de Torrejón a Ajalvir, km 4, 28850, Torrejón de Ardoz, Spain

[25] NRC Herzberg Astronomy and Astrophysics, 5071 West Saanich Road, Victoria, BC V9E 2E7, Canada

[26] Department of Physics and Astronomy, University of Victoria, Victoria, BC V8P 5C2, Canada

[27] Université de Bordeaux – CNRS Laboratoire d'Astrophysique de Bordeaux, 33600 Pessac, France

[28] Institut de Radioastronomie Millimétrique, 38406 Saint-Martin d'Hères, France

[29] Instituto de Radioastronomía y Astrofísica, Universidad Nacional Autónoma de México, A.P. 3-72 (Xangari), 8701 Morelia, Mexico

[30] Instituto de Astronomía, Univ. Nacional Autonoma de Mexico, Ciudad Universitaria, A.P. 70-264, Cuidad de Mexico 04510, Mexico

[31] Institute of Astronomy and Astrophysics, Academia Sinica, 11F of Astronomy-Mathematics Building, AS/NTU No.1, Sec. 4, Roosevelt Rd., Taipei 10617, Taiwan, R.O.C.

[32] Division of Science, National Astronomical Observatory of Japan, 2-21-1 Osawa, Mitaka, Tokyo 181-8588, Japan

[33] Institute of Low Temperature Science, Hokkaido University, N19W8, Kita-ku, Sapporo, Hokkaido 060-0819, Japan

[34] Department of Physics, The University of Tokyo, 7-3-1, Hongo, Bunkyo-ku, Tokyo 113-0033, Japan

[35] Yukawa Institute for Theoretical Physics, Kyoto Univ. Oiwake-cho, Kitashirakawa, Sakyo-ku, Kyoto-shi, Kyoto-fu 606-8502, Japan

[36] Departament de Quíñmica, Universitat Autònoma de Barcelona, 08193 Bellaterra, Spain

[37] Graduate School of Informatics and Engineering, The University of Electro-Communications, Chofu, Tokyo 182-8585, Japan

[38] Department of Astronomy, The University of Texas at Austin, 2515 Speedway, Austin, TX 78712, USA

[39] Steward Observatory, 933 N Cherry Ave., Tucson, AZ 85721, USA

[40] Star and Planet Formation Laboratory, RIKEN Cluster for Pioneering Research, Wako, Saitama 351-0198, Japan

[41] SOKENDAI (The Graduate University for Advanced Studies), Shonan Village, Hayama, Kanagawa 240-0193, Japan

Appendix A: Details on data reduction
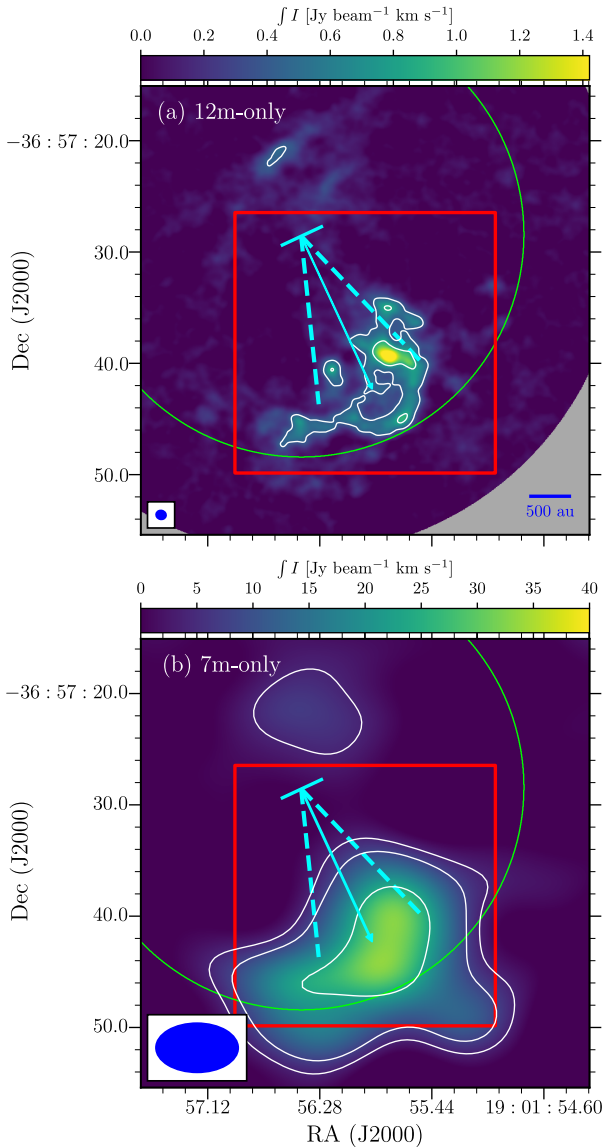
Fig. A.1. Moment 0 of CH_3OH ($4_{2,3}$-$3_{1,2}$) E as observed with (a) the 12m ALMA main array, and (b) with ACA only. The white contours mark the [5, 10, 30]σ emission. The green semicircle shows the ALMA Band 6 FoV of the combined data (see Figure 2). The grey background delimits the region inside each ALMA pointing, while the red square outline the region shown in each panel in Figure 2. The ALMA beam is shown in the lower left corners.

Table A.1 summarises the details of the dataset acquired with ALMA for the CrA stellar cluster in the context of the FAUST Large Program (see Codella et al. 2021). The B6 data were acquired over 12 spectral windows (SPWs) with a bandwidth ($\Delta\nu$)/frequency resolution ($\delta\nu$) of 59 MHz/122 kHz ($\sim$67-82 km s^{-1}/0.17-0.20 km s^{-1}), whilst 6 SPWs of 59 MHz/61 kHz ($\sim$160-190 km s^{-1}/0.20 km s^{-1}) were observed in B3. In all spectral settings, one additional SPW of 1.9 GHz was dedicated to the thermal dust continuum emission, i.e. 2294 (B6s1), 2404 (B6s2), and 5917 km s^{-1} (B3). For the latter, $\delta\nu$ was 0.5 MHz for B6s1 (0.72 km s^{-1}) and B3 (1.54 km s^{-1}), and 1.1 MHz (1.39 km s^{-1}) for B6s2. Details of the observations and of the calibrators are summarised in Table A.1. The average angular scales covered at these frequencies range from a synthesised

Table A.1. Technical details of the FAUST observations.

Fields	Band 3 (B3)	Band 6 (B6s1)	Band 6 (B6s2)
ν range (GHz)	85.0-89.0, 97.0-101.0	214.0-219.0, 229.0-234.0	242.5-247.5, 257.2-262.5
Configurations	C3-C6	C1-C4	C1-C4
B_{min}-B_{max}	9–1400 m	9–1400 m	15–3600 m
ACA	No	Yes	Yes
Antennas[a]	47	45–48(12)	45–48(12)
$\Delta\nu$ (SPW-lines)[b]	59 MHz $\sim$175 km s^{-1}	59 MHz $\sim$75 km s^{-1}	59 MHz $\sim$75 km s^{-1}
$\delta\nu$ (SPW-lines)[b]	61 kHz $\sim$0.2 km s^{-1}	122 kHz $\sim$0.17 km s^{-1}	122 kHz $\sim$0.17 km s^{-1}
$\langle\theta_{res}\rangle$[c]	0.40$''$ × 0.27$''$	0.42$''$ × 0.34$''$	0.41$''$ × 0.30$''$
$\langle\theta_{MRS}\rangle$[c]	27$''$	19$''$	17$''$
Calibrators	J1924-2914, J1925-3401, J1937-3958	J1924-2914, J2056-4714, J1957-3845	J1802-3940, J1924-2914, J2056-4714

Notes. [a] Parenthesis refer to the number of antennas for ACA. Ranges are given when multiple execution blocks are employed; [b] $\Delta\nu$ and $\delta\nu$ are the typical bandwidth and spectral resolution of SPWs dedicated to line observations; [c] Synthesised beam ($\theta_{res} = \lambda/B_{max}$) and maximum recoverable scale ($\theta_{MRS} = 0.6\,\lambda/B_{min}$) in the combined 12 m and ACA data sets;

beam, θ_{res}, of $\sim$0$''$.4×0$''$.3 to a maximum recoverable scale, θ_{MRS}, of $\sim$21$''$; that is, $\sim$52-2700 au at the source distance of 130 pc (Lindberg et al. 2014). The final datacubes were obtained combining different ALMA configurations, including the 12m array and the ACA. Figure A.1 shows an example of how the distribution of CH_3OH ($4_{2,3}$-$3_{1,2}$) E, observed in B6-s1, varies with the array used.

After the data were calibrated (Sect. 2), we followed a two-step deconvolution procedure for imaging: (*i*) An initial deconvolution was performed with a relatively low threshold ($\sim$4.5 times the dirty noise) and without masking the emission. A reference mask was generated applying the same threshold to the image obtained in this way. (*ii*) Then, a second deconvolution cycle was performed using the mask generated in step-*i* as starting point for the AUTO-MULTITHRESH option in TCLEAN. This two-step procedure ensures that all channels, including those with strong spatial filtering, have been properly masked.

## Appendix B: Additional notes and results

B.1. Source properties at 1.3 mm

We used the 2D Gaussian fit algorithm provided by CASA (The CASA Team 2022) to analyse the 1.3 mm continuum maps (see Section 3.1) and extract the properties of each source identified in the CrA cluster.

The fitting algorithm provided the positions of the continuum peaks of each source, the intensity of the continuum peaks, $\mathcal{F}_{1.3mm}^{max}$, and the integrated flux density, $\int \mathcal{F}_{1.3mm}\, d\Omega$, over a circular region encompassing the entire 3σ continuum emission. A summary of these parameters is presented in Table B.1.

### B.2. Channel maps, velocity structures, and spectra

In this subsection we report the channel maps of CH_3OH ($4_{2,3}$-$3_{1,2}$) and p-H_2CO ($3_{0,3}$-$2_{0,2}$) and the integrated intensity maps of the blueshifted and redshifted components of SiO (5-4) emission, respectively, in Figures B.1(a,b), and B.2. The velocity

(a)

(b)
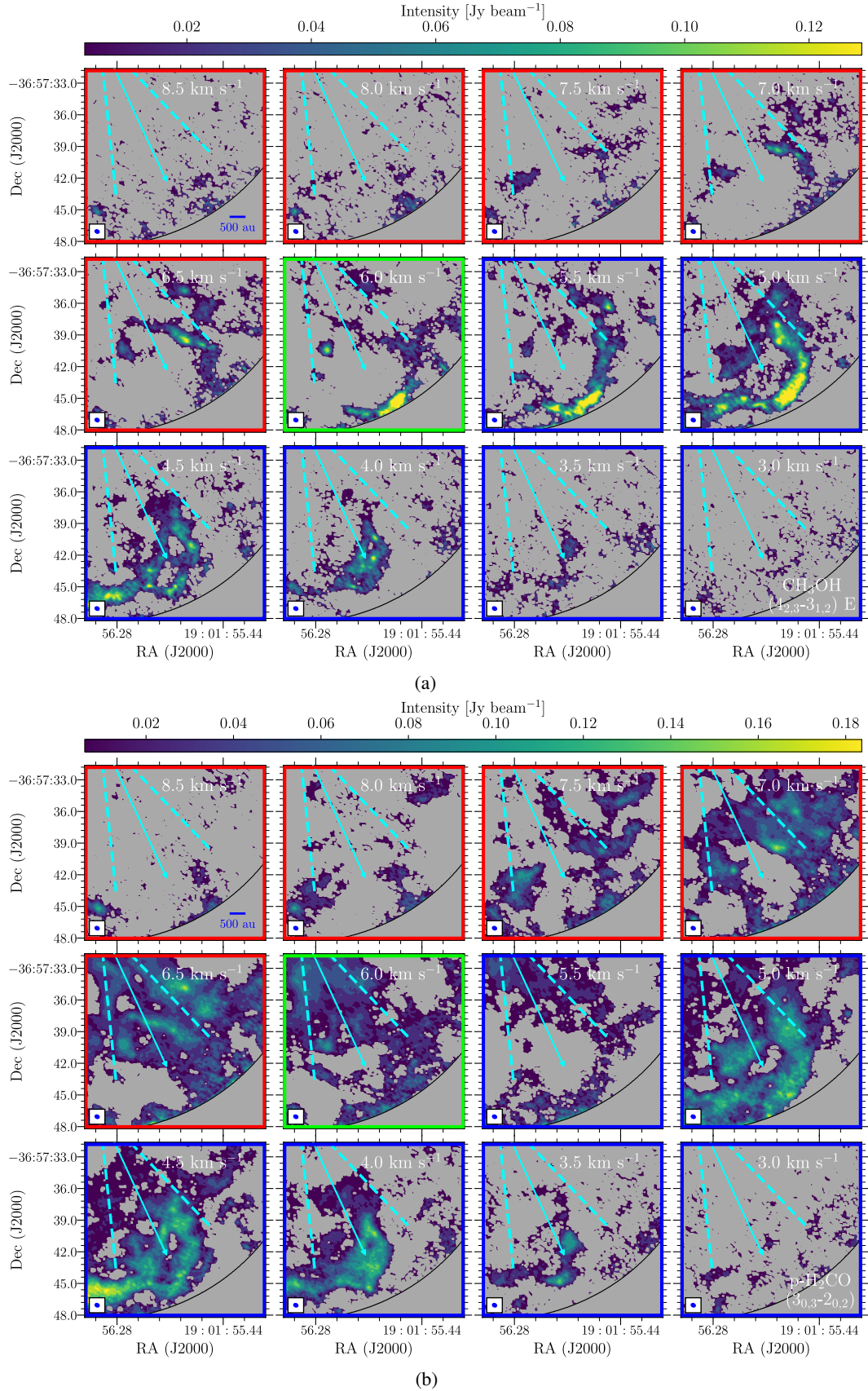
Fig. B.1. Velocity channel maps of (a) CH$_3$OH (4$_{2,3}$-3$_{1,2}$) E and (b) p-H$_2$CO (3$_{0,3}$-2$_{0,2}$). The green framed panel marks the systemic velocity of IRS7B, while the blue- and red- framed panels represent the blueshifted and redshifted components of the emission, respectively. The emission was masked at 3σ, and the colour bar peaks at 75σ, where the average 1σ noise in each channel is (a) 1.2 mJy beam^{-1} and (b) 2 mJy beam^{-1}. The black arc shows the ALMA Band 6 FoV. Each panel reports the corresponding velocity. (a) Channel map of CH$_3$OH (4$_{2,3}$-3$_{1,2}$) E (b)Channel map of p-H$_2$CO (3$_{0,3}$-2$_{0,2}$)

Table B.1. Source properties derived at 1.3 mm.

Source-ID	α_{ICRS} hh:mm:ss.ss	δ_{ICRS} dd:mm:ss.ss	$\mathcal{F}_{1.3mm}^{max}$ mJy/beam	$\int \mathcal{F}_{1.3mm}\,d\Omega$ mJy
IRS7B	19:01:56.42	-36:57:28.58	190	304
SMM 1C	19:01:55.30	-36:57:17.23	97	269
IRS7A	19:01:55.33	-36:57:22.60	17	20
CXO 34	19:01:55.79	-36:57:28.23	16	16
FAUST-5	19:01:56.63	-36:57:40.49	4	4
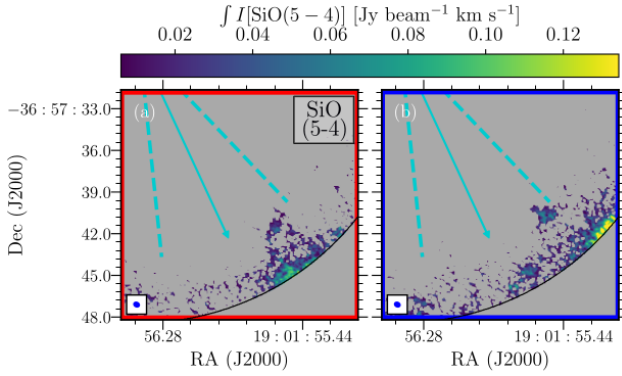
Fig. B.2. Integrated intensity maps of the blueshifted and redshifted components of SiO emission (panels a and b, respectively). The blueshifted and redshifted components were derived by integrating the emission at $> 3\sigma$ in the velocity ranges of ~[6.7, +12] km s^{-1} and ~[0, +6.2] km s^{-1}, respectively. The black arc shows the ALMA Band 6 FoV.

structures defined by the three molecular tracers are masked at the 3σ level. The green framed panels in Figure B.1 indicate the systemic velocity of IRS7B, while the blue- and red-framed panels represent the blueshifted and redshifted components of the emission, respectively. The same colour code was used in Figure B.2.

Figures B.1(a,b) show one velocity channel in steps of three original spectral resolution elements, while in Figure B.2 we show the integrated blueshifted and redshifted components of SiO (5-4) in the velocity ranges of ~[+6.7, +12] km s^{-1} and ~[0, +6.2] km s^{-1}, respectively. Cyan lines and arrows follow Figure 1, and trace the supposed outflow cavity walls detected at 1.3 mm with ALMA (Section 4). Notably, the region shown in Figure B.2 is the only part of the ALMA FoV where extended integrated SiO emission is observed.

Figure B.3 shows the spectra of all the observed lines extracted at three positions along the arc structure, centred at the peak positions of CH$_3$OH ($4_{2,3}$-$3_{1,2}$), SiO (5-4) and p-H$_2$CO ($3_{0,3}$-$2_{0,2}$), labelled A, B and C, respectively. The targeted lines are detected with a signal-to-noise ratio of $>3\sigma$. The exceptions are the CH$_3$OH-A ($3_{1,3}$-$4_{0,4}$) at position B and the SiO (5-4) at position C, where we derived 3σ upper limits (Table 1). All the CH$_3$OH and H$_2$CO lines observed with a spectral resolution of ≤ 0.5 km s^{-1} show double-peaked profiles, with the redshifted component associated with extended envelope emission, and the blueshifted one due to the arc (see Appendix B). We used the Python Spectroscopic Toolkit (PySpecKit; Ginsburg et al. 2022) to fit the spectra assuming two Gaussian components. In regions B and C, the blueshifted lines have peak velocities of ~+5 km s^{-1} and a narrow FWHM of ~1 km s^{-1}. The red components are centred at +6.6 km s^{-1}, and have FWHMs of between 1 and 1.2 km s^{-1}. The low-frequency methanol lines (E_{up} = 22 K, and 84 K) observed with a spectral resolution of 1.54 km s^{-1} show single Gaussian-like profiles. The lines peak between +5.7 and +6.3 km s^{-1}, close to V_{sys}^{IRS7B}. The detection of a single Gaussian line in the low-resolution data is due to the coarse spectral resolution. On the other hand, the line width of SiO at position B is ~ 3.5 km s^{-1}.

The integrated line intensities of the multiple CH$_3$OH transitions were used to construct rotational diagrams and quantify the column density and rotational temperature of CH$_3$OH along the molecular arc (see Sect. 3.3).
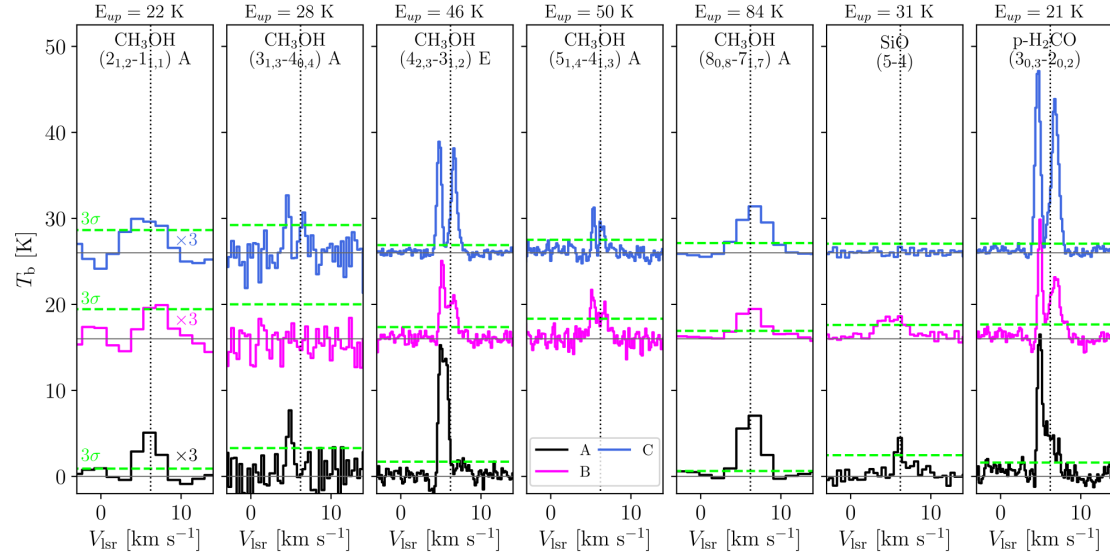
Fig. B.3. Spectral overview of the tracers listed in Table 1 extracted at the three positions labeled A, B, and C in Fig. 2a. The extraction regions have an equivalent area of nine beams. Vertical lines report the $V_{\rm sys}^{\rm IRS7B}$ (+6 km s^{-1}; Lindberg et al. 2014, and Ohashi et al. 2023), grey lines mark the zero-level of each spectrum, while green dashed lines show the 3σ level.